Nanoscale Potential Fluctuations in Zirconium Oxide and the Flash Memory Based on Such Fluctuations

Gritsenko, V. A.; Perevalov, T. V.; Kruchinin, V. N.; Aliev, V. S.; Gerasimova, A. K.; Erenburg, S. B.; Trubina, S. V.; Kvashnina, K. O.; Prosvirin, I. P.;

Originally published:

July 2018

Advanced Electronic Materials 4(2018)9, 1700592

DOI: https://doi.org/10.1002/aelm.201700592

Nanoscale Potential Fluctuations in Zirconium Oxide and the Flash Memory Based on Such Fluctuations

V.A. Gritsenko[1,2,3], T.V. Perevalov[1,2], V.N. Kruchinin[1], V.S. Aliev[1], A.K. Gerasimova[1]

[1] Rzhanov Institute of Semiconductor Physics, SB RAS, 13 Acad. Lavrent'ev Ave., 630090, Novosibirsk, Russia

[2] Novosibirsk State University, 2 Pirogov Str., 630090, Novosibirsk, Russia

[3] Novosibirsk State Technical University, 20 K. Marx Ave., 630073, Novosibirsk, Russia

S.B. Erenburg[4,5], S.V. Trubina[4], K.O. Kvashnina[6]

[4] Nikolaev Institute of Inorganic Chemistry SB RAS, 3 Acad. Lavrent'ev Ave., 630090 Novosibirsk, Russia

[5] Budker Institute of Nuclear Physics SB RAS, 11 Acad. Lavrent'ev Ave., 630090 Novosibirsk, Russia

[6] HZDR, Institute of Resource Ecology, 01314 Dresden, Germany

I.P. Prosvirin[7]

[7]Boreskov Institute of Catalysis SB RAS, 5 Acad. Lavrent'ev Ave., 630090 Novosibirsk, Russia

X-ray photoelectron spectroscopy, EXAFS, XANES, spectral ellipsometry and quantum-chemistry calculations were used to examine the atomic and electronic structure of non-stoichiometric amorphous ZrO_x slightly enriched with zirconium. The experimental data show that the ZrO_x material consists of stoichiometric ZrO_2, metallic Zr and zirconium suboxides ZrO_y. The structure of ZrO_x is analyzed using the Random Bonding and Random Mixture models. A model of nanoscale spatial potential fluctuations in ZrO_x is substantiated. In this model, the potential fluctuations for electrons and holes arise due to the local fluctuations of bandgap energy in the range from 0 to 5.4 eV. A ZrO_x-based flash memory element with giant retention time is proposed.

For five decades, silicon oxide SiO_2 and silicon nitride Si_3N_4 have been two key dielectrics in silicon-based devices. Presently, both are being replaced with high-κ dielectrics, like HfO_2, ZrO_2,

Ta_2O_5 and Al_2O_3[1, 2]. Slightly non-stoichiometric, metal-enriched high-κ dielectrics are examined as a storage medium in charge-trap flash memory devices. Oxygen vacancies and oxygen polyvacancies in high-κ dielectrics are used as traps in those devices [3]. It is believed that oxygen vacancies play a key role in dielectric reversible switching between states with low and high resistance under current pulse (resistive effect). Intensive studies aimed at the development of resistive random-access memory (ReRAM) are carried out now[4-6]. ReRAM have attracted great attention due to their simple structure, low power consumption, high-speed operation, high-density integration, multibyte switching. A number of binary metal oxides have been investigated for ReRAM applications. Non-stoichiometric zirconium oxide (ZrO_x) is one of the promising materials for ReRAM[7-9].

The atomic and electronic structure of ZrO_2 was studied experimentally[10-15] and theoretically[14, 16-19]. The study of nonstoichiometric zirconium oxide ZrO_x is of much interest from the viewpoint of fundamental knowledge. A variation of the chemical composition (stoichiometry) of ZrO_x leads to a dramatic change of the electronic structure of the material, thus offering a possibility to control its physical (optical and electric) properties.

The purpose of the present study was to investigate the atomic and electronic structure of nonstoichiometric zirconium oxide ZrO_x to justify the nanoscale potential fluctuations caused by a fluctuationing of spatial chemical composition.

The Structure of ZrO_x

According to reflection high-energy electron diffraction (RHEED) data, all the ZrO_x films were amorphous. Surface field emission scanning electron microscopy (FESEM) images of the ZrO_x films are shown in Fig. 1. Evidently, the variation of the nanoscale uniformity of ZrO_x films with a change of stoichiometry «x» is observed. In ZrO_x films (x=1.4) heavily enriched with the metal, metallic of round-shaped Zr clusters were identified. The diameters of the clusters ranged in the interval from 2 to 20 nm, the mean diameter being about 10 nm (Fig. 1a). In the images, the clusters look as bright round points. With increasing the oxygen concentration in the films, the

light spots grow in sizes, and their diameter increases to 20 nm (Fig. 1b,1c). Nearly stoichiometric films look uniform (Fig. 1d).

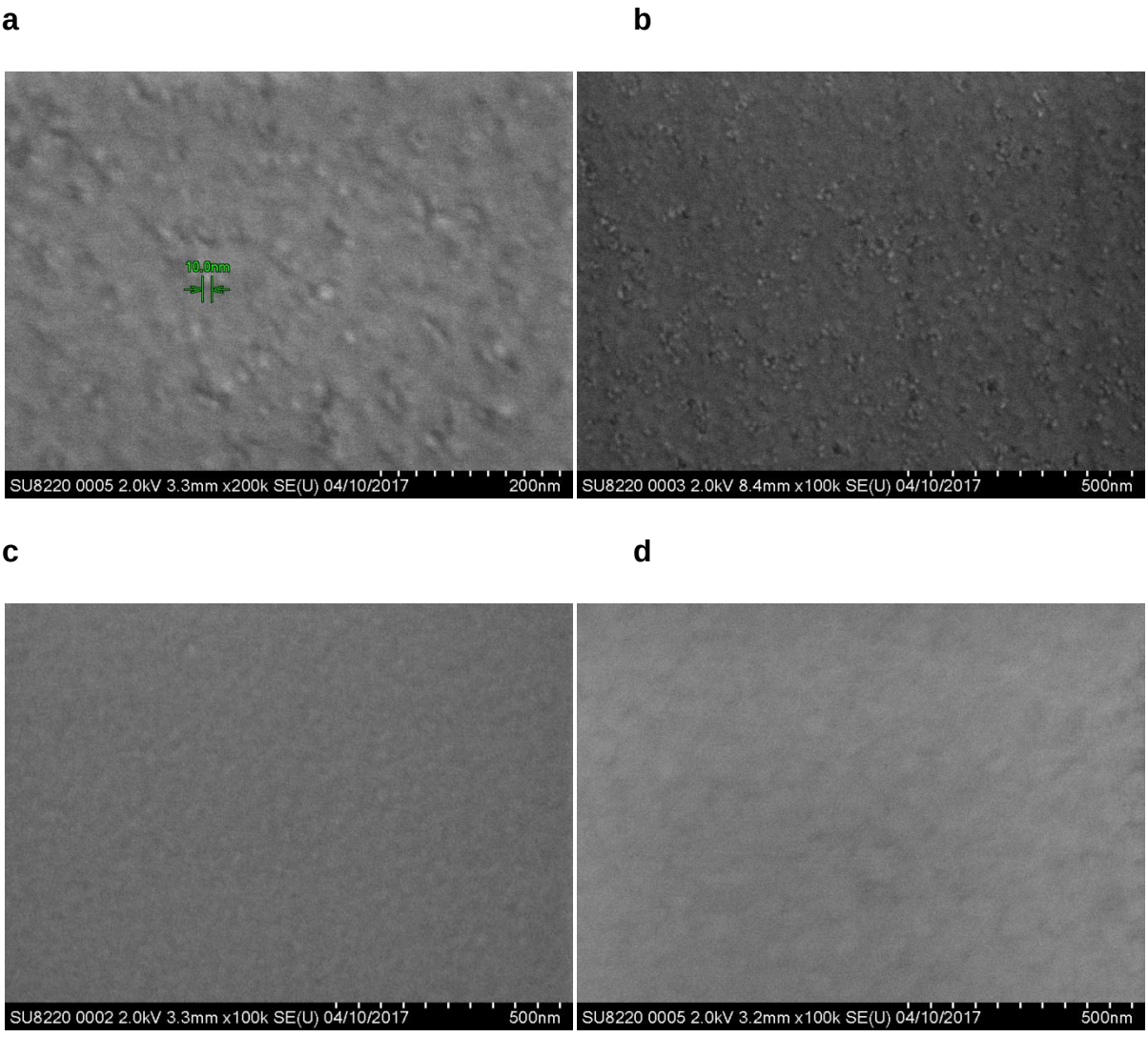

Figure 1 | FESEM-images of the ZrO_x film surface. The metallic Zr clusters are seen as light round spots against the dark background. (a), (b) – $ZrO_{1.4}$ at different scales, (c) – $ZrO_{1.7}$, (d) – ZrO_2.

The X-ray photoelecrton spectra (XPS) of the Zr $3d_{3/2,5/2}$ level in nearly stoichiometric zirconium oxide, in non-stoichiometric $ZrO_{1.7}$ enriched with the metal and in metallic Zr are shown in Fig. 2a. The deconvolution of the experimental $ZrO_{1.7}$ spectrum has shown that the dominating high-energy signal was due to stoichiometric ZrO_2, whereas the low-energy signal pointed to the presence of zirconium suboxides (ZrO_y) (Fig.2). $ZrO_{1.7}$ enriched with the metal exhibited three

signals, two signals being due to stoichiometric ZrO_2 and due to ZrO_y, respectively, and the third low-energy signal due to metallic Zr. The peak deconvolution due to the Zr $3d_{3/2,5/2}$ level in ZrO_x shows that $ZrO_{1.7}$ contains ≈10% of metallic Zr, ≈15% of ZrO_y and ≈75% of ZrO_2.

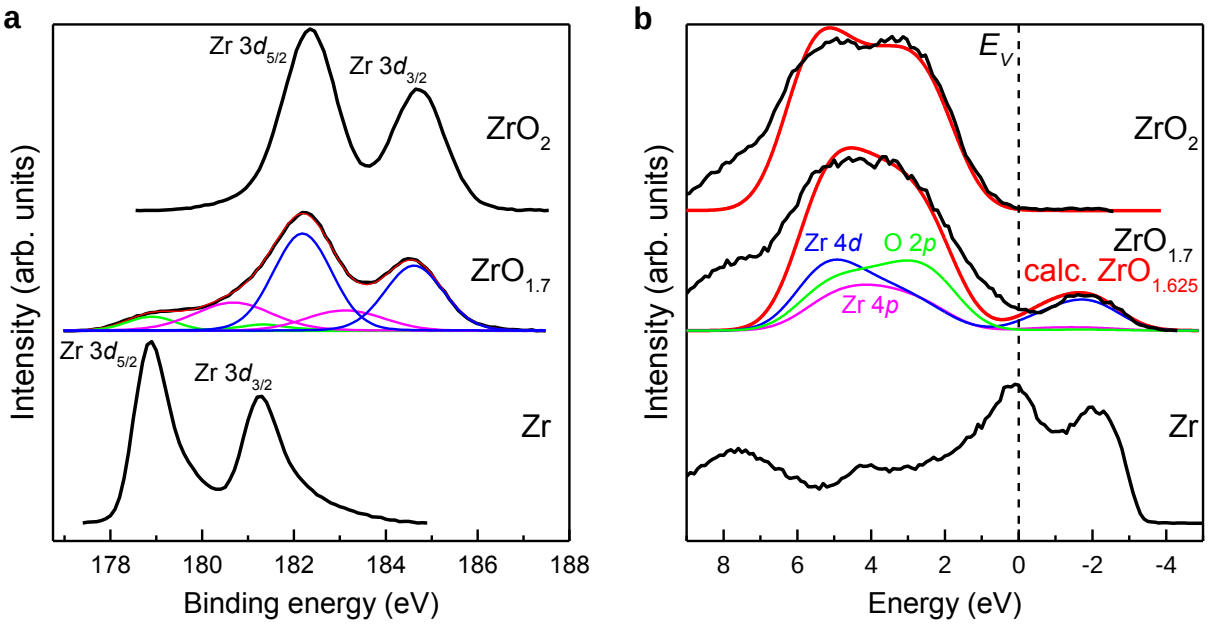

Figure 2 | X-ray Photoelectron Spectra. (a) The peak due to the Zr 3*d* level in ZrO_2, $ZrO_{1.7}$, and in Zr (black curves). The color curves show the $ZrO_{1.7}$ spectra decomposition into Gaussian functions: the blue curve refers to ZrO_2; the purple curve refers to ZrO_y; the green curve - to Zr; and the red curve - to the sum of all the four components. (b) The experimental, and calculated (black and red curves, respectively) valence-band XPS of ZrO_2, $ZrO_{1.7}$ and Zr. The top of the valence band E_V is set to zero energy. The thin color curves indicate the type of the atomic orbitals (Zr 4*d*, Zr 4*p*, and O 2*p*) of which the XPS of $ZrO_{1.625}$ is formed.

The experimental and calculated valence-band XPS of ZrO_2, $ZrO_{1.7}$ and metallic Zr are shown in Fig. 2b. A proof for the presence of oxygen vacancies in ZrO_x is the formation in the valence-band XPS of a peak with a maximum at an energy approximately 2 eV higher than the valence-band top E_V (Fig. 2b). The position of the peak, as well as its width and intensity, well comply

with the calculated XPS for m-ZrO_2, in which, per each 24 atoms there are three oxygen vacancies that form deep occupied defect states in the band gap. The deconvolution of the calculated spectrum of ZrO_x into the contributions due to individual atomic orbitals shows that the main contributions to the ZrO_x valence-band XPS are due to the 4*d* and 4*p* states of zirconium and due to the 2*p* states of oxygen (Fig. 2b). The peak above the valence-band top is almost completely formed by the 4*d* states of zirconium.

The spectral dependences of the absorption coefficient in ZrO_2, $ZrO_{1.7}$ and in Zr are shown in Fig.3a. The fundamental absorption edge in stoichiometric ZrO_2 at the energy of 5.0 eV. The optical absorption in $ZrO_{1.7}$ monotonically increases in the energy range from 1.2 to 5.0 eV. Similar behavior is also observed in Zr. Thus, the optical absorption in $ZrO_{1.7}$ is due to the metallic phase.

The spectral dependence of the refraction index in ZrO_2, $ZrO_{1.7}$ and in Zr is shown in Fig. 3b. In ZrO_2, the "normal" refraction-index dispersion is observed. In the range of quantum energies from 1.2 to 5.0 eV, the refraction index monotonically increases in the value from 2.10 to 2.58 with the increasing quantum energy (Fig. 3b). Such behavior is characteristic for dielectrics at quantum energies lower than the bandgap E_g. In $ZrO_{1.7}$, an "abnormal" refractive index dispersion typical of metals is observed. The refractive index magnitude monotonically decreases as the quantum energy increases in the range from 1.2 to 5.0 eV. Similar behavior is also observed in Zr (Fig. 3b).

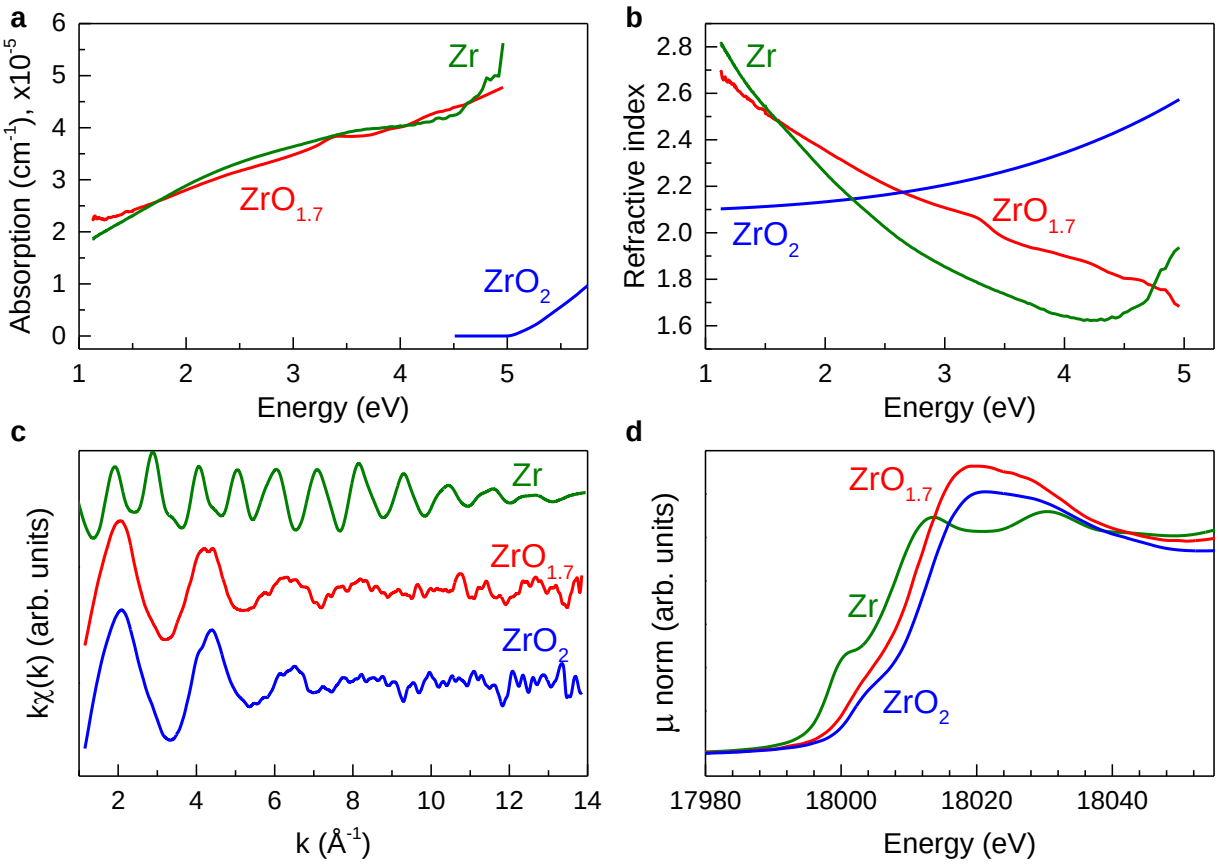

Figure 3 | Optical and Zr *K* edge X-ray absorption spectra of $ZrO_{1.7}$, Zr and in ZrO_2. (a) Spectral dependence of the absorption coefficient α (for ZrO_2 taken from ref. [20]). (b) Spectral dependence of the refractive index *n*. (c) EXAFS and (d) XANES spectra.

According to ref. 10-12, 15, ZrO_2 has several polymorphic modifications. Only monoclinic (m-) ZrO_2 is stable at room temperature. As a starting structural model for the examined material, we used the monoclinic structure[21]. In m-ZrO_2, a zirconium atom is surrounded by seven oxygen atoms. The experimental Zr *K* edge X-ray absorption spectra is shown in Fig. 3c, d. A very significant disordering of the structure is observed for samples of oxides prepared without annealing (Fig. 3c). In the process of modeling extended X-ray absorption fine structure (EXAFS) ZrO_2 spectra, the coordination number for oxygen atoms was fixed, $N_{Zr\text{-}O}$= 7, and seven shortest separations Zr-O (average value $R_{Zr\text{-}O}$=2.140 Å) and one (average) separation $R_{Zr\text{-}Zr}$=3.31 Å were calculated. As a result of studying the simulation, it was found that, in the ZrO_x sample, the mean Zr-O separation was $R_{Zr\text{-}O}$=2.135 Å and the oxygen coordination number proved to be $N_{Zr\text{-}O}$=5.7,

which value was smaller than the coordination number in ZrO_2 (probably, due to oxygen vacancies).

From Fig. 3d, it is seen that the absorption edge of ZrO_x X-ray Absorption Near Edge Structure (XANES) spectra is shifted to lower energies with respect to ZrO_2; the difference between the energy positions of the absorption edges in ZrO_2 and ZrO_x is about 1 eV. Such a shift corresponds to an average charge at Zr atoms in the examined ZrO_x films being reduced in comparison with the Zr charge in ZrO_2. The latter can be indicative of both the presence of excess Zr in the oxides, in which the first coordination sphere of zirconium has the composition $Zr_\upsilon O_{6+\upsilon}$ with $\upsilon \leq 1$ (since the average stoichiometric formula is $ZrO_{1.7}$), and the presence of a small quantity of a metal phase (<10%).

For simplicity, consider the structure of ZrO_x with the example of the simplest cubic phase. The cubic phase of ZrO_2 consists of ZrO_8 structural units. The replacement of one oxygen atom with a zirconium atom results in the formation of a $ZrZrO_7$ structural unit, whereas the replacement of two, three, or four oxygen atoms with two, three, or four zirconium atoms, respectively, yields $ZrZr_2O_6$, $ZrZr_3O_5$, or $ZrZr_4O_4$ structural units, respectively. Hypothetically, in a similar manner, $ZrZr_5O_3$, $ZrZr_6O_2$, $ZrZr_7O$, and $ZrZr_8$ structural units can be formed. However, the replacement of more than four oxygen atoms with zirconium atoms turns out to be impossible because of geometric limitations. The radius of the oxygen atom is 0.48 Å, whereas the radius of the zirconium atom is 2.06 Å. According to the EXAFS data, the length of the Zr-O bond is 2.135 Å. As a result, the replacement of a larger amount of oxygen with zirconium atoms for an eight-coordinated central zirconium atom turns out to be impossible.

In the Random Bonding model, ZrO_x consist of a random mixture of $ZrZr_\upsilon O_{8-\upsilon}$ structural units with υ=0, 1, 2, 3, 4, 5, 6, 7 and 8. Such a model fails to describe the ZrO_x structure. In the Random Mixture model, ZrO_x presents a mixture of ZrO_2 and Zr. The experiment points to the presence of ZrO_2 and Zr in ZrO_x; however, XPS and data point to the occurrence of ZrO_y suboxides involving $ZrZr_\upsilon O_{8-\upsilon}$ structural units as well. Thus, neither the Random Bonding model nor the Random

Mixture model adequately describes the structure of ZrO_x. According to the experimental data, the ZrO_x consists of $ZrZr_\upsilon O_{8-\upsilon}$ structural units; however, the distribution of the structural units in the material is not a random one like the distribution that appears in the Random Bonding model.

The model of nanoscale potential fluctuations in ZrO_x

Below, we substantiate an Intermediate Model for the ZrO_x structure. According to the XPS, EXAFS and spectral ellipsometry data, ZrO_x consists of ZrO_2, Zr and a small amount of ZrO_y suboxides. ZrO_y may appear at the ZrO_2/Zr interface, in the volume of ZrO_2 and in the volume of the Zr. A two-dimensional representation of the ZrO_x structure in the Intermediate Model is shown in Fig. 4a.

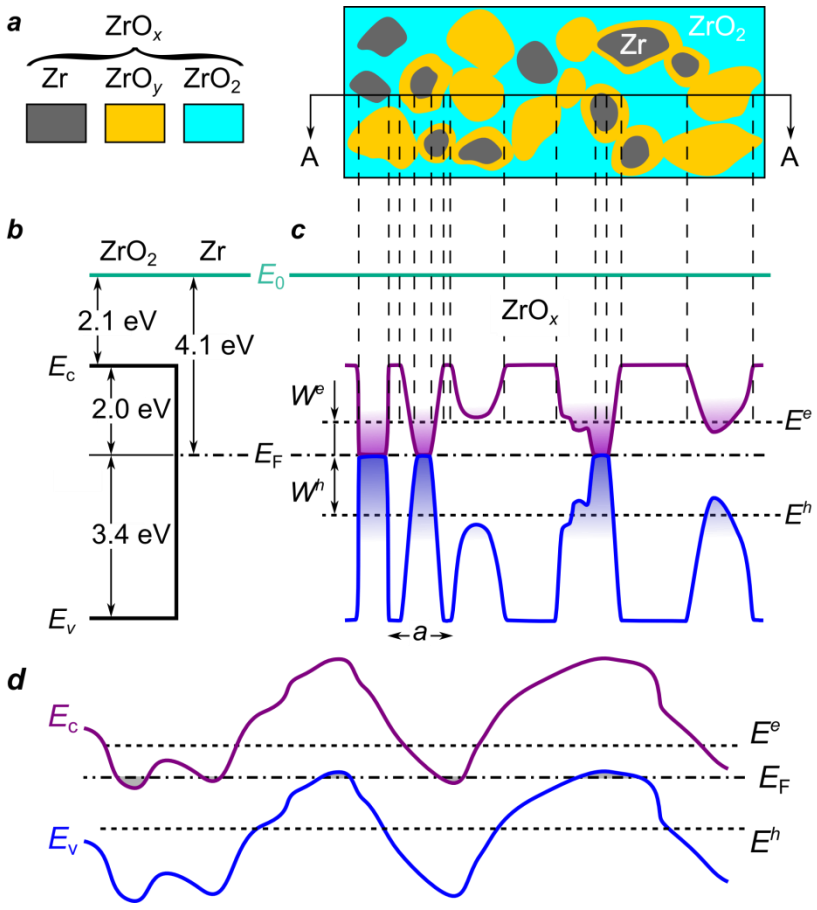

Figure 4 | The Intermediate Model of nanoscale potential fluctuations in non-stoichiometric ZrO_x. (a) Two-dimensional model for the structure of ZrO_x. (b) The energy diagram of the Zr/ZrO_2

interface: the green solid horizontal line shows the electron energy with respect to one in vacuum E_0, and the dash-and-dot line shows the position of Fermi level E_F in Zr. (c) One-dimensional model for potential fluctuations in ZrO_x: E^e and E^h are the percolation levels for electrons and holes; W^e and W^h are the barriers for excitation of electrons and holes from the Fermi level to the electron and hole percolation levels, respectively; a is the characteristic spatial scale of potential fluctuations; (d) One-dimensional Shklovskii-Efros model for potential fluctuations in doping-compensated semiconductors; E_F is the Fermi level in the semiconductor; E^e and E^h are the percolation levels for electrons and holes[22].

According to this model, ZrO_x consists of three phases: ZrO_2, ZrO_y and Zr. The band diagram of ZrO_x is shown in Fig. 4b. The bandgap energy of ZrO_2 is E_g=5.4 eV[23]. The electron affinity of ZrO_2 is χ=2.1 eV[23]. The work function of metallic Zr is 4.1 eV. According to the Intermediate Model, spatial fluctuations of the chemical composition give rise to the local spatial fluctuations of the bandgap energy in ZrO_x (Fig.4c). E_g in ZrO_x varies in the range from 0 to 5.4 eV. The conduction-band edge position, with respect to the electron energy in vacuum E_0, varies in the range from 2.1 eV to 4.1 eV. The latter quantities define the maximum fluctuation scale of conduction-band-edge energy position E_c in ZrO_x. The energy position of valence-band top, with respect to the electron energy in vacuum, varies in the range from 4.1 eV to 7.5 eV. The height of the potential barrier for holes at the Zr/ZrO_2 interface defines the maximum fluctuation scale of the valence-band top position E_v in ZrO_x. According to the structural measurements, the typical spatial scale of potential fluctuations in ZrO_x falls into the range from 2 nm to 20 nm (see Fig. 1).

The possibility of using ZrO_x as a storage medium in flash memory devices

The operating principle of state-of-the-art flash memory devices is based on the accumulation (localization) of electrons or holes at deep traps in silicon nitride[24, 25]. The lifetime of electrons and holes in localized states amounts to 10 years at 85 ^oC. According to Fig. 4, metallic zirconium clusters in a ZrO_2 matrix act as deep potential wells (traps) for contact-injected electrons and holes.

Thus, there arises a possibility to use, as the storage medium in flash memory elements, instead of silicon nitride, nonstoichiometric ZrO_x slightly enriched with the metal (see Fig. 5).

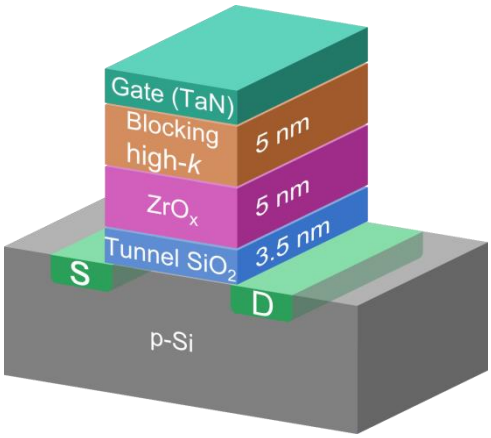

Figure 5 | A flash memory element using ZrO_x as the storage medium.

According to Fig. 4, the depth of the potential wells due to metallic Zr for electrons and holes in ZrO_x is 2.0 and 3.4 eV. For comparison, the energies of the electron and hole traps in silicon nitride are equal to 1.4 eV[26]. Thus, it can be expected that the potential wells due to metallic Zr in ZrO_x will be capable of ensuring a giant retention time, or giant lifetime of electrons/holes in localized states.

The flash memory element is similar to the traditional field-effect transistor (FET) in which, instead of the gate dielectric, a three-layer dielectric is used (Fig. 5). A thermally grown 3.5-nm thick silicon oxide layer functions as the tunnel dielectric. Over the tunnel oxide, a 5-nm thick storage layer of ZrO_x is provided. Over the storage dielectric, a low-conducting blocking high-κ dielectric is used. As the latter dielectric, Al_2O_3 is appropriate for use[24]. Tantalum nitride TaN is normally used in state-of-the-art flash memory elements as a conducting gate.

On the application of a negative voltage pulse to the gate, the injection of holes from the silicon through the tunnel oxide leads to the injected holes trapping at the metallic clusters in ZrO_x. As a result, a positive charge gets accumulated in ZrO_x. This positive charge attracts the electrons

at the silicon/tunnel oxide interface, and an inversion charge due to electrons forms in the silicon. The inversion layer forms a conducting channel that connects the source and the drain. Here, the FET resistance is low, and this state corresponds to logic "zero". Since the metallic clusters in ZrO_x act as deep traps, the lifetime of electrons in a localized state is large, exceeding ten years.

On the application of a positive voltage pulse to the gate in the flash memory element, the electrons tunneling from the silicon through the tunnel oxide become trapped at the metallic clusters in ZrO_x. A negative charge accumulated in the storage medium (ZrO_x) attracts holes in the silicon substrate, and the conducting channel vanishes. The FET resistance here is high, corresponding to logic "unity". Such a state can be stored during more than ten years. Thus, the proposed flash memory element has two stable states: "zero" and a "unity".

According to Fig.4, the depth of the potential well for electrons and holes due to metallic Zr in ZrO_x amounts, respectively, to 2.0 and 3.4 eV. For comparison, the energies of electron and hole traps in silicon nitrides amount to 1.4 eV. An estimation shows that the lifetime for an electron trapped at zirconium at temperature 150 ^oC is approximately one hundred years. Thus, the "metallic" potential wells in ZrO_x are capable of ensuring a giant retention time in such flash memory devices.

Discussion

ZrO_x consists of stoichiometric ZrO_2, metallic Zr and zirconium suboxides ZrO_y. XPS and EXAFS experiments are indicative of the presence of stoichiometric ZrO_2. The presence of metallic Zr is evidenced by XPS and spectral ellipsometry data. XPS and XANES data point to the presence of ZrO_y suboxides in ZrO_x.

The large radius of the zirconium atom, 2.06 Å, in comparison with the radius of the oxygen atom, 0.48 Å, makes the formation of $ZrZr_\upsilon O_{8-\upsilon}$ structural units with $\upsilon>4$ impossible. Indeed, because of the large radius of the zirconium atom, the formation of Zr-O bonds with a bond length in the interval of 2.03 to 2.27 Å becomes improbable. That is why the clusters of ZrO_2 and Zr with

a small fraction of ZrO_y suboxides, consisting of $ZrZr_\upsilon O_{8-\upsilon}$ structural units with $\upsilon<4$, form in the material.

In the Shklovskii-Efros model, the potential fluctuations have an electrostatic nature, and they are due to the spatial fluctuations of the concentrations of charged donors and acceptors in perfectly compensated semiconductors[22]. In the latter case, the bandgap energy remains unchanged, and the built-in electric field promotes a spatial separation of the electron and holes.

In the model of potential fluctuations in non-stoichiometric ZrO_x proposed in the present paper, the local spatial potential fluctuations for electrons and holes are due to the local fluctuations of bandgap energy. Unlike in the Shklovskii-Efros model, the neutrality at each point of the space is in ZrO_x. The second difference is that the local electric fields for electrons and holes are directed in one and the same direction, promoting the localization of the charge carriers of both types at one and the same spatial point. Previously, the model of potential fluctuations due to the local spatial fluctuations of the chemical composition was substantiated for nonstoichiometric SiO_x[25-27] and for nonstoichiometric SiN_x[27-29]. The difference between the models of potential fluctuations in tetrahedral nonstoichiometric silicon nitride and oxide consists in that the minimum local bandgap energies in SiN_x and SiO_x are equal to the bandgap energy of silicon (for crystalline and amorphous Si, we have respectively E_g=1.1 and 1.6 eV[30]), whereas the minimum local bandgap energy of ZrO_x is equal to zero.

References

1. Robertson, J. & Wallace, R.M. High-K materials and metal gates for CMOS applications. *Materials Science and Engineering: R: Reports* **88**, 1-41 (2015).
2. Perevalov, T.V. & Gritsenko, V.A. Application and electronic structure of high-permittivity dielectrics. *Physics-Uspekhi* **53**, 561-575 (2010).
3. Gritsenko, V.A., Perevalov, T.V. & Islamov, D.R. Electronic properties of hafnium oxide: A contribution from defects and traps. *Physics Reports* **613**, 1-20 (2016).

4. Lee, M.J. et al. A fast, high-endurance and scalable non-volatile memory device made from asymmetric Ta_2O_{5-x}/TaO_{2-x} bilayer structures. *Nature Materials* **10**, 625-630 (2011).

5. Wang, Z.R. et al. Memristors with diffusive dynamics as synaptic emulators for neuromorphic computing. *Nature Materials* **16**, 101-108 (2017).

6. Wedig, A. et al. Nanoscale cation motion in TaO_x, HfO_x and TiO_x memristive systems. *Nature Nanotechnology* **11**, 67-75 (2016).

7. Wu, X. et al. Reproducible unipolar resistance switching in stoichiometric ZrO_2 films. *Applied Physics Letters* **90**, 183507 (2007).

8. Wang, S.Y., Lee, D.Y., Tseng, T.Y. & Lin, C.Y. Effects of Ti top electrode thickness on the resistive switching behaviors of rf-sputtered ZrO_2 memory films. *Applied Physics Letters* **95**, 112904 (2009).

9. Lee, J. et al. Effect of ZrO_x/HfO_x bilayer structure on switching uniformity and reliability in nonvolatile memory applications. *Applied Physics Letters* **97**, 172105 (2010).

10. Li, P., Chen, I.W. & Pennerhahn, J.E. X-Ray-Absorption Studies of Zirconia Polymorphs .1. Characteristic Local Structures. *Physical Review B* **48**, 10063-10073 (1993).

11. Li, P., Chen, I.W. & Pennerhahn, J.E. X-Ray-Absorption Studies of Zirconia Polymorphs .2. Effect of Y_2O_3 Dopant on ZrO_2 Structure. *Physical Review B* **48**, 10074-10081 (1993).

12. Li, P., Chen, I.W. & Pennerhahn, J.E. X-Ray-Absorption Studies of Zirconia Polymorphs .3. Static Distortion and Thermal Distortion. *Physical Review B* **48**, 10082-10089 (1993).

13. Rush, G.E., Chadwick, A.V., Kosacki, I. & Anderson, H.U. An EXAFS study of nanocrystalline yttrium stabilized cubic zirconia films and pure zirconia powders. *Journal of Physical Chemistry B* **104**, 9597-9606 (2000).

14. Shaposhnikov, A.V. et al. The atomic and electron structure of ZrO_2. *Journal of Experimental and Theoretical Physics* **102**, 799-809 (2006).

15. Soo, Y.L. et al. Local structures surrounding Zr in nanostructurally stabilized cubic zirconia: Structural origin of phase stability. *Journal of Applied Physics* **104**, 113535 (2008).

16. Stapper, G., Bernasconi, M., Nicoloso, N. & Parrinello, M. Ab initio study of structural and electronic properties of yttria-stabilized cubic zirconia. *Physical Review B* **59**, 797-810 (1999).

17. Rignanese, G.M., Detraux, F., Gonze, X. & Pasquarello, A. First-principles study of dynamical and dielectric properties of tetragonal zirconia. *Physical Review B* **64**, 134301 (2001).

18. Medvedeva, J.E., Freeman, A.J., Geller, C.B. & Rishel, D.M. Screened-exchange determination of the electronic properties of monoclinic, tetragonal, and cubic zirconia. *Physical Review B* **76**, 235115 (2007).

19. Jiang, H., Gomez-Abal, R.I., Rinke, P. & Scheffler, M. Electronic band structure of zirconia and hafnia polymorphs from the GW perspective. *Physical Review B* **81**, 085119 (2010).

20. Zhu, L.Q. et al. Spectroscopic ellipsometry characterization of ZrO_2 thin films by nitrogen-assisted reactive magnetron sputtering. *Materials Science in Semiconductor Processing* **9**, 1025-1030 (2006).

21. Smith, B.D.K. & Newkirk, H.W. The Crystal Structure of Baddeleyite (Monoclinic ZrO_2) and its Relation to the Polymorphism of ZrO_2. *Acta Cryst.* **18**, 983-991 (1965).

22. Shklovskii, B.I. & Efros, A.L. Percolation Theory and Conductivity of Highly Inhomogeneous-Media. *Uspekhi Fizicheskikh Nauk* **117**, 401-435 (1975).

23. Afanas'ev , V.V. Internal Photoemission Spectroscopy: Principles and Applications (Elsevier, Amsterdam, 2008).

24. Gritsenko, V.A. in Thin Films on Si: Electronic and Photonic Applications (eds. Narayanan, V., Frank, M. & Demkov, A.A.) 273-322 (World Scientific Press, 2016).

25. Prince, B. Vertical 3D Memory Technologies (2014).

26. Gritsenko, V.A., Perevalov, T.V., Orlov, O.M. & Krasnikov, G.Y. Nature of traps responsible for the memory effect in silicon nitride. *Applied Physics Letters* **109**, 062904 (2016).

27. Gritsenko, V.A. Atomic structure of the amorphous nonstoichiometric silicon oxides and nitrides. *Physics-Uspekhi* **51**, 699-708 (2008).

28. Gritsenko, V.A. et al. Silicon dots/clusters in silicon nitride: photoluminescence and electron spin resonance. *Thin Solid Films* **353**, 20-24 (1999).

29. Sorokin, A.N., Karpushin, A.A. & Gritsenko, V.A. Electronic structure of SiN_x. *Jetp Letters* **98**, 709-712 (2014).

30. Park, N.M., Choi, C.J., Seong, T.Y. & Park, S.J. Quantum confinement in amorphous silicon quantum dots embedded in silicon nitride. *Physical Review Letters* **86**, 1355-1357 (2001).

Acknowledgements

This work was supported in part by the Russian Foundation for Basic Research (Grant No. 16-02-00175a, EXAFS spectroscopy) and by the Russian Science Foundation (Grant No. 14-19-00192, quantum chemistry, model of potential fluctuations, flash memory element). The simulation study was performed on the computer cluster of ISP SB RAS. The authors are grateful to YA Zhivodkov for samples FESEM measurements at the 'Nanostructures' Collective Use Center (ISP SB RAS, Novosibirsk).

Author contributions

V.A. Gritsenko designed the study and developed the nanoscale potential fluctuations model and flash memory element based on ZrO_x. T.V. Perevalov performed quantum-chemical simulations. V.N. Kruchinin carried out the spectroellipsometric measurements. V.S. Aliev and A.K. Gerasimova synthesized the samples. S.B. Erenburg, S.V. Trubina, K.O. Kvashnina performed and analyzed EXAFS and XANES experiments. I.P. Prosvirin performed XPS measurements.

Methods

Sample preparation. Thin (~50 nm) ZrO_x (x<2) films were prepared using Ion Beam Sputtering Deposition (IBSD[31]) on the «Spector» installation (Veeco, USA) on the pre-prepared silicon wafers (Si(100), n-type, ρ=4.5 Ω×cm). Before deposition, the substrates were precleaned in a hydrofluoric acid (HF) solution. The metallic zirconium (Zr>99.9%) target was sputtered by Ar^+ ions with the energy of 1.2 keV and a current density on the target surface of about 1 $mA \cdot cm^{-2}$ in the presence of high purity oxygen (O_2 >99.999%). The growth chamber was pre-pumped up to a pressure of ~10^{-5} Pa before argon and oxygen flow feeding. The pressure in the growth chamber during the zirconium oxide deposition process was about 1.5×10^{-2} Pa. The zirconia films synthesis rate was controlled by using quartz sensor MAXTEC-400. The substrate was initially at room temperature and it did not exceed ~70 °C during the film growth process. The oxygen content in the ZrO_x was varied by changing the O_2 partial pressure using the gas flow controller.

Film morphology. The ZrO_x morphology was investigated by the reflection high-energy electron diffraction (RHEED) technique on an EF-Z4 device at the accelerating voltage of 50 kV. The nanoscale visualization of film surfaces was carried out using a scanning electron microscope (SEM) Hitachi-su-8220 with a field emission cathode (FESEM) by using a secondary electron detector SE(U) at magnifications Mag=5kx,10kx,20kx,60kx. The accelerating voltage was 2 kV. The distance from the tip of the objective lens to the sample surface (WD) was 3.5 mm. The instrumental microscope resolution was about 0.8 nm at 15 kV.

X-ray photoelecrton spectroscopy. The X-ray photoelecrton spectra (XPS) measurements were performed on a SPECS machine equipped with an X-ray source with a twin Al/Ag anode, an ellipsoidal crystal X-ray monochromator FOCUS-500, a PHOIBOS 150 hemispherical electron energy analyzer and an ion source. The spectra were obtained using the monochromatic Al $K\alpha$

radiation ($h\nu$ = 1486.74 eV) and the fixed analyser pass energy of 20 eV under ultrahigh vacuum conditions. The binding energy was calibrated using the C 1*s* peak at 284.8 eV related to adventitious hydrocarbons for the as-inserted surface. To damp the surface charging effect, the low energy electron gun FG-20 (I = 0.8 мA, E = 2 eV) was used. The relative element content ([O]/[Zr] atomic ratio) was defined using the detailed spectra of Zr 3*d* and O 1*s* and the known element sensitivity factors[32]. To define the integrated peak intensity correctly, the background was subtracted by the Shirley method.

X-ray absorption spectroscopy. Extended X-ray Absorption Fine Structure (EXAFS) and X-ray Absorption Near Edge Structure (XANES) measurements were performed assisted with the European Synchrotron Radiation Facility (ESRF) at beamline BM20. The incident energy was selected using the Si(111) double crystal monochromator. Higher harmonics rejection was achieved by two mirrors with Rh surfaces. The size of the X-ray beam was 5 mm (horizontal) x 0.2 mm (vertical). The XAFS (X-ray Absorption Fine Structure) spectra were measured in the fluorescence mode using a 12-element Ge detector. The incident flux of X-ray quanta on the Zr *K* edge was ~1×10^{10} ph\s. The incident angle on the sample was ~1º. Three scans of EXAFS data (from 250 eV below to 800 eV aboe Zr *K* edge (17998 eV)) were collected at room temperature. It should be noted that the signal-to-noise ratio for the spectra of the studied samples is small; after 10 $Å^{-1}$, reliable EXAFS modulations are practically absent, which objectively testifies the structural disorder of the samples (amorphous, multiphase, nonstoichiometric, vacancy in the structure).

The EXAFS spectra were analysed by the Artemis and Athena software[33]. The Fourer transformations of EXAFS oscillation were carried out within 3.0 – 11.0 $Å^{-1}$. The fitting was performed in the R-range of 1.0 – 3.1 Å with k- and k^2-weights. The EXAFS amplitudes and phase-shifts were calculated by FEFF (an automated code for *ab initio* calculations of XAFS)[34] for the

crystallographic data[35]. The fitting quality was estimated by the difference between the model and experimental Fourier transformed EXAFS function (*R*-parameter).

Spectroellipsometry. The optical properties (refractive index $n(\omega)$ and absorption coefficient $\alpha(\omega)$ dispersion), as well as film thicknesses, were determined by spectroscopic ellipsometer «SPECTROSCAN» (produced by ISP SB RAS). The spectral dependences of the ellipsometrical angles Ψ and Δ were measured in wavelength range λ = 250–900 nm. The spectral resolution of the instrument was 2 nm, the recording time of one spectrum was in no excess of 20 s, the angle of incidence of the light beam was 70°. We used a four-zone measurement technique followed by averaging over all four zones. The solution of the inverse problem of ellipsometry and fitting the spectral dependences of the ellipsometrical angles $\Psi(\lambda)$ and $\Delta(\lambda)$ were performed in accordance with the basic equation of ellipsometry:

$$\mathrm{tg}\,\Psi \cdot \mathrm{e}^{\mathrm{i}\Delta} = \frac{\mathrm{R_p}}{\mathrm{R_s}}\,, \qquad (1)$$

Here R_p and R_s are the complex light reflection coefficients for the waves polarized in the incidence plane and perpendicular to the plane, respectively. These coefficients depend on the optical constants and layer thicknesses. To calculate the dispersion dependences of refractive index $n(\lambda)$ and absorption coefficient $k(\lambda)$, a model of semi-infinite reflecting medium (an isotropic substrate – air) was employed. Thus, in the whole spectral range, the spectral dependences of polarization angles were fitted for *m* points of the spectrum by minimizing the error function:

$$\sigma^2 = \frac{1}{m} \cdot \sum_{i=1}^{m} \left[\left(\Delta_{\mathrm{exp.}} - \Delta_{calc.} \right)^2 + \left(\Psi_{\mathrm{exp.}} - \Psi_{calc.} \right)^2 \right] \qquad (2)$$

$\Psi(\lambda)$ and $\Delta(\lambda)$ were also fitted using the approximate dispersion model proposed by Lorentz and Drude. The dispersion dependences calculation are performed independently for each spectrum point.

Quantum chemistry. Quantum-chemistry calculations were performed for monoclinic (m-) ZrO_2. Simulations were performed in terms of the hybrid density functional theory (DFT) in the periodic supercells model using a B3LYP functional in the Quantum-ESPRESSO code[36].

Hybrid exchange-correlation functional B3LYP was adopted to reproduce the correct zirconium oxide band gap value 5.5 eV. The calculations were made using the following electronic configuration of the constituent elements: Zr [Ar] $4s^2 4p^6 5s^2 5d^2$ and O [He] $2s^2\ 2p^4$, where the core configurations are shown in the parentheses. The potentials of nuclei and core electrons were described by atomic norm-conserving pseudopotentials. The plane-wave cutoff energy was selected to ensure the convergence of the total cell energy to 0.005 eV/atom and was taken equal to 80 Ry. The oxygen-depleted non-stoichiometric zirconium oxides were simulated by a oxygen atoms removing and a subsequent relaxation of all atoms in the 24-atom supercell. The valence band XPS were calculated by summing the partial densities of states of the valence orbitals taken with the weight factors equal to the corresponding photoionization cross-sections[37], with Gauss function broadening with the FWHM of 0.7 eV.

References

31. Shvets, V.A. et al. Electronic structure and charge transport properties of amorphous Ta_2O_5 films. Journal of Non-Crystalline Solids **354**, 3025-3033 (2008).

32. Scofield, J.H. Hartree-Slater subshell photoionization cross-sections at 1254 and 1487 eV. Journal of Electron Spectroscopy and Related Phenomena **8**, 129-137 (1976).

33. Ravel, B. & Newville, M. ATHENA, ARTEMIS, HEPHAESTUS: data analysis for X-ray absorption spectroscopy using IFEFFIT. Journal of Synchrotron Radiation **12**, 537-541 (2005).

34. Rehr, J.J. & Albers, R.C. Theoretical approaches to x-ray absorption fine structure. Reviews of Modern Physics **72**, 621-654 (2000).

35. Smith, B.D.K. & Newkirk, H.W. The Crystal Structure of Baddeleyite (Monoclinic ZrO2) and its Relation to the Polymorphism of ZrO_2. Acta Cryst. **18**, 983-991 (1965).

36. Giannozzi, P. et al. QUANTUM ESPRESSO: a modular and open-source software project for quantum simulations of materials. J Phys Condens Matter **21**, 395502 (2009).

37. Yeh, J.J. Atomic Calculation of Photoionization Cross-Section and Asymmetry Parameters (Gordon and Breach Science Publishers, Langhorne, PE (USA), 1993).